ARTICLE OPEN

Electromagnetic signatures of a chiral quantum spin liquid

Saikat Banerjee [1], Wei Zhu[2,3] and Shi-Zeng Lin [4,5] ✉

Quantum spin liquids (QSL) have emerged as a captivating subject within interacting spin systems that exhibit no magnetic ordering even at the lowest temperature accessible experimentally. However, definitive experimental evidence remains elusive. In light of the recent surge in theoretical and experimental interest in the half-filled Hubbard model on a triangular lattice, which offers the potential for stabilizing a chiral QSL, we investigate the electromagnetic signatures of this phase to facilitate experimental detection. Utilizing a combination of parton mean-field theory and unbiased density-matrix renormalization group calculations, we systematically examine the electrical charge and orbital electrical current associated with a spinon excitation in the chiral QSL. Additionally, we calculate the longitudinal and transverse optical conductivities below the Mott gap. Furthermore, employing quantum field theory analysis, we unravel the connection between spinon excitations and emergent as well as physical gauge fields. Our results demonstrate that the chiral QSL phase exhibits a distinct electromagnetic response, even within a Mott insulator regime. This finding holds great potential for enabling the experimental detection of this long-sought-after phase.

INTRODUCTION

Quantum spin liquid (QSL) states are described by interacting quantum spin systems that abstain from magnetic ordering even at absolute zero temperature. This absence of magnetic ordering provides a ground state characterized by quantum disorder, featuring distinctive long-range quantum entanglement, fractionalized excitations, and the emergence of associated gauge fields. As a result, understanding and characterizing QSL has been a challenge since its inception[1]. The experimental identification of QSL states is rendered even more intricate due to the absence of a conventional order parameter[2]. However, recent advances on both the theoretical and experimental fronts have spurred a continuous surge of interest in analyzing and detecting this elusive state of matter[3]. Examples span from the identification of various iridates/ruthenates compounds as promising candidates to realize proximate Kitaev physics[4–8], to the observation of topological spin liquids in Rydberg atom quantum simulators[9] and quantum processors[10]. The manifestation of QSL necessitates the suppression of magnetic orders, making frustrated magnets a fruitful ground for looking for QSL. In this context, the triangular lattice Hubbard model (TLHM) has consistently occupied a prominent role of interest.

In the limit of large U in the TLHM at half-filling, the effective low-energy Hamiltonian transforms into an antiferromagnetic Heisenberg model, consequently stabilizing the conventional 120° (Néel) order[11–15]. However, the prevailing notion is that as the correlations weaken while remaining above the Mott transition, the ground state of the TLHM transitions to a quantum spin liquid (QSL) state through a quantum phase transition[16]. In particular, a series of density-matrix renormalization group studies (DMRG)[17–20], as well as matrix product state (MPS)[21] analyses on TLHMs, have recently pointed towards the emergence of evidence for chiral quantum spin liquid (cQSL) phases of the Kalmeyer–Laughlin type[22,23]. We refer to Fig. 1 for an illustrative schematic of the phase diagram.

The TLHM finds experimental realization in specific materials. Previous experimental investigations have provided distinctive indications of a QSL phase within particular organic Mott insulators[24–27]. Nonetheless, a debate persists regarding the gapped[26] or gapless[28] characteristics of the underlying excitations. In the context of another material adopting a triangular lattice structure, namely $NaYbO_2$, the gapless nature finds robust support from various specific heat measurements[29,30]. However, experiments with nuclear magnetic resonance[31] or muon spin rotation[32] support the gapless nature in triangular lattice material YbMgGaO$_4$, although the true nature of the magnetic ground state in YbMgGaO$_4$ remains a controversial topic possibly related to the unavoidable presence of disorder in this material. Furthermore, supporting evidence emerges from neutron scattering studies, revealing the existence of a spinon Fermi surface[33]. Therefore, the quest for definitive unmistakable signatures capable of unraveling the genuine essence of the QSL phase remains crucial.

Inspired by the identification of the cQSL phase in TLHM and its potential relevance in several compounds, here, we systematically analyze its electromagnetic responses. Despite being a Mott insulator, there is a remnant electromagnetic response due to the virtual hopping of electrons[34,35]. Assuming the presence of a spontaneously broken time-reversal symmetry (TRS) in a cQSL phase, we analyze the corresponding effective spin model[18] within the framework of the parton mean-field spinon description. This analysis yields insights into the associated orbital magnetization and electrical polarization. Moreover, we perform unbiased density matrix renormalization group (DMRG) calculations on the half-filled TLHM at an intermediate coupling U ($U_1 < U < U_2$). The results of our numerical examination confirm the mean-field results concerning the electromagnetic responses. To establish a comprehensive and universally applicable perspective, we invoke a quantum field theory description to explicitly elucidate the interplay between the emergent and physical gauge fields and the low-energy spinon excitations within the cQSL.

[1]Theoretical Division, T-4, Los Alamos National Laboratory, Los Alamos, NM 87545, USA. [2]School of Science, Westlake University, No. 600 Dunyu Road, 310030 Hangzhou, China. [3]Key Laboratory for Quantum Materials of Zhejiang Province, Westlake University, 310024 Hangzhou, China. [4]Theoretical Division, T-4, and CNLS, Los Alamos National Laboratory, Los Alamos, NM 87545, USA. [5]Center for Integrated Nanotechnologies (CINT), Los Alamos National Laboratory, Los Alamos, NM 87545, USA. ✉email: szl@lanl.gov
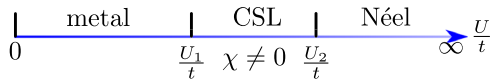
Fig. 1 A schematic phase diagram for the triangular lattice Hubbard model at half-filling. The phase diagram contains a metallic phase at small U, followed by a putative cQSL phase with non-vanishing chiral order parameter $\chi = \langle \mathbf{S}_i \cdot (\mathbf{S}_j \times \mathbf{S}_k) \rangle$ at an intermediate coupling regime $U_1 \sim 9t$, and $U_2 \sim 11t$[17,20], and a magnetic ordered Néel state at strong coupling. Note that $\chi = 0$ in the other two phases.

To relate our theoretical framework to experiments, we compute the transverse optical conductivity (within the spinon description), which is associated with the magneto-optical Faraday rotation (MOFE)

$$\Theta_F = \frac{l}{nc} \sigma'_{xy}(\Omega), \tag{1}$$

where l is the thickness in the direction of light propagation with frequency Ω, n is the index of refraction, and $\sigma'_{xy}(\Omega)$ is the real part of the optical conductivity in 3D. Our electromagnetic response functions, including the orbital magnetization profile and the structure of Θ_F, provide a clear experimental signature of the cQSL. For completeness, we also analyze the behavior of the dynamic spin-structure factor and lay out the possible connection with the relevant experiments. It is worth noting that the real component of the Hall optical conductivity, assessed through the MOFE angle in experimental observations, is proportional to the imaginary component of susceptibility (see the Supplementary Material for more details). This observation stands in stark contrast to various other response functions, where the dissipative part (imaginary component of the Hall conductivity) is measured.

The rest of this paper is organized as follows: in section "Results," we provide the spinon description of the cQSL in TLHM. In sections "Analysis" and "Case of a localized spinon," we provide details of the derivation for electrical polarization and orbital magnetization. The DMRG calculations supporting our mean-field calculations are given in section "DMRG calculations." Section "Quantum field theory description" provides a picture based on quantum field theory. In sections "Dynamic spin-structure factor" and "Optical conductivity and Faraday rotation," we compute the dynamic spin structure factor and transverse optical conductivity with the electrical polarization, respectively. Finally, we discuss the implications of our results and conclude in section "Discussion."

RESULTS

Model Hamiltonian

We start with the TLHM at half-filling with the corresponding Hamiltonian written as

$$\mathcal{H}_0 = -t \sum_{\langle ij \rangle, \sigma} c^\dagger_{i\sigma} c_{j\sigma} + U \sum_i n_{i\uparrow} n_{i\downarrow}, \tag{2}$$

where $c^\dagger_{i\sigma}$ creates an electron at site i with spin σ, and U is the strength of the onsite Coulomb repulsion. In the strong coupling limit ($U \gg t$), the charge degrees of freedom are gapped out, and the relevant microscopic model can be analyzed in terms of an effective spin model. Within a second-order perturbation expansion in t/U, the corresponding spin Hamiltonian reads $\mathcal{H}_{\text{eff}} = J^{(2)} \sum_{\langle ij \rangle} \mathbf{S}_i \cdot \mathbf{S}_j$, where $J^{(2)} = 4t^2/U$ is the antiferromagnetic Heisenberg coupling. However, in the intermediate coupling regime, i.e., $U \gtrsim t$, the above second-order perturbation does not completely capture the low-energy dynamics, and we need to include higher-order spin corrections. Such a procedure leads to further neighbor spin exchange terms, including ring exchange-like interactions[36]. Therefore, although a Néel order is preferred at larger U, incorporating subleading order correction modifies the overall magnetic order at an intermediate U. Previous theoretical

works[34,37–39] have reported the existence of two critical coupling strengths $U_1 \sim 9t$, and $U_2 \sim 11t$. The current consensus is that TLHM hosts a putative QSL phase in the intermediate regime between U_1 and U_2, eventually becoming a Néel ordered state at a larger $U > U_2$.

Motivated by these previous studies and recent developments in the DMRG results[17,20], we adopt a *phenomenological* chiral spin liquid model to describe its concomitant features. The effective Hamiltonian, which hosts cQSL as a ground state, is written as

$$\mathcal{H}_{\text{csl}} = \tilde{J} \sum_{\langle ij \rangle} \mathbf{S}_i \cdot \mathbf{S}_j + \tilde{J}_\chi \sum_{\langle\langle ijk \rangle\rangle} \mathbf{S}_i \cdot (\mathbf{S}_j \times \mathbf{S}_k), \tag{3}$$

where the associated exchange couplings are written in terms of the parameters of the original low-energy spin model. Here, $\langle ij \rangle$ denotes the nearest sites, and $\langle\langle ijk \rangle\rangle$ denotes three sites in a unit triangle. It was argued in refs. [18,34] that the four-spin ring exchange term (see Supplementary Material (SM) for details) is responsible for the appearance of the chiral term in Eq. (3).

Here, we focus on the model as in Eq. (3) and analyze it within a mean-field description. We utilize the standard parton decomposition of the spins as $\mathbf{S}_i = \frac{1}{2} f^\dagger_{ia} \boldsymbol{\sigma}_{\alpha\beta} f_{i\beta}$, where $f^\dagger_{ia}$ creates a neutral spinon excitation with spin α at site i, and $\boldsymbol{\sigma}$ denotes the vector of Pauli matrices (the repeated indices are assumed to be summed over). This fractionalization leads to an enlargement of the Hilbert space. Therefore, one needs to implement a local constraint ($f^\dagger_{ia} f_{ia} = 1$) to project to the physical Hilbert space. Plugging this back into Eq. (3) and assuming a nonzero mean-field decomposition as $m_{ij} = \langle f^\dagger_{ia} f_{ja} \rangle$, we obtain a noninteracting spinon Hamiltonian as (see the Supplementary Material for more details)

$$\mathcal{H} = -\frac{\tilde{J}}{2} \sum_{\langle ij \rangle} m_{ji} f^\dagger_{ia} f_{ja} + \frac{3i\tilde{J}_\chi}{16} \sum_{\langle ij \rangle}' \left(m_{ik} m_{kj} f^\dagger_{ja} f_{ia} - \text{h.c.} \right), \tag{4}$$

where the primed summation corresponds to all the permutations between the three neighboring sites i, j, k. Here, we adopted a mean-field decomposition only in the particle-hole channel, although a more general decomposition with both the particle-particle and particle-hole channel may provide a *qualitatively* better description of the emergent spinon spectrum[40,41].

Assuming translational invariance, we simplify the mean-field order parameter $m_{ij} = m_0 e^{i\phi_{ij}}$, where m_0 is the amplitude and ϕ_{ij}'s are bond-dependent phases. Subsequently, we capture the physics of the Hamiltonian in Eq. (4) with a simplified model as

$$\mathcal{H} = -\tilde{t} \sum_{\langle ij \rangle} e^{i\psi_{ij}} f^\dagger_{ia} f_{ja} + \text{h.c.}. \tag{5}$$

Focusing on a three-site cluster, the hopping amplitude $\tilde{t}$, and the phases ψ_{ij}'s are related to the parameters in Eq. (4) as

$$\tilde{t} \cos \psi_{ij} = \frac{\tilde{J} m_0}{2} \cos \phi_{ji} + \frac{3\tilde{J}_\chi m_0^2}{16} \sin(\phi_{ik} + \phi_{kj}), \tag{6}$$

$$\tilde{t} \sin \psi_{ij} = \frac{\tilde{J} m_0}{2} \sin \phi_{ji} + \frac{3\tilde{J}_\chi m_0^2}{16} \cos(\phi_{ik} + \phi_{kj}), \tag{7}$$

However, the phases ψ_{ij}'s and the hopping $\tilde{t}$ remain undetermined. To make further progress, we utilize a variational flux state, such that the spinons hopping on the decorated two-sublattice structure realizes a π-flux per plaquette [see Fig. 2a] with the hopping amplitudes between different neighboring sites such that the total flux within the rhombus-shaped unit cell is π[21]. In such a construction, we can do further simplification and solve Eqs. (6), and Eq. (7) to show that (see the Supplementary Material for more details)

$$\tilde{t} = \frac{\tilde{J} m_0}{2} + \frac{3\tilde{J}_\chi m_0^2}{16}, \quad \psi_{ij} = -\phi_{ij} \tag{8}$$

with the constraint, the total flux within a triangle is $\pi/2$. Note that m_0 still remains undetermined. A particular choice of ψ_{ij} is shown

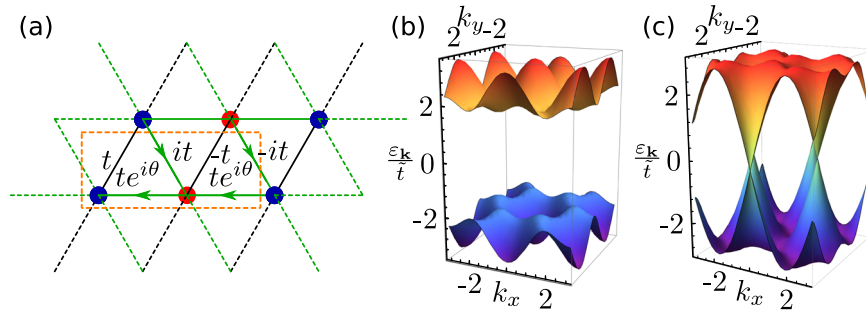**Fig. 2 Phenomenological spinon tight-binding model on a triangular lattice and its dispersion. a** Phenomenological spinon model on a triangular lattice with bond-dependent hoppings and a two-sublattice unit cell illustrated within the orange-dashed box. The hopping phases allow π-flux within each rhombus-shaped bipartite plaquette (see the main text for more discussion). For $\theta = 0$, both the *up* and a *down* triangle forming the rhombus acquire uniform $\pi/2$ fluxes, where the flux configuration is staggered for any nonzero θ. The spinon spectrum for the uniform (gapped, $\theta = 0$) and the staggered (gapless, $\theta = \pi/2$) flux configuration are shown in (**b, c**), respectively.

in Fig. 2a to realize the staggered flux configurations between the up and the down triangles, where $\theta = 0$ corresponds to $\pi/2$ flux within a triangle. TRS is preserved for $\theta = \pi/2$.

Diagonalizing the Hamiltonian in Eq. (5) obtains the corresponding spinon band structure. The uniform flux phase ($\theta = 0$) leads to a gapped spinon spectrum, as shown in Fig. 2b. Note that the spectrum becomes gapless for the staggered flux configuration with $\theta = \pi/2$, and remains gapped for any other choice of θ. The spinon spectrum is doubly degenerate for the spin-up and spin-down components. The gapped bands acquire a nonzero Chern number in the uniform flux configuration. Using the link variable formulation[42], we obtain the total Chern number distribution for the bands as $\mathcal{C} = \{1, -1\}$ in the cQSL phase. Therefore, it is expected to host *chiral* spinon edge modes and exhibit quantized Hall thermal conductivity at low temperatures[43].

Analysis

Now we discuss the main results of this paper by focusing on the electromagnetic signatures in the cQSL phase. Despite a charge-neutral Mott insulator, the virtual hopping of electrons leads to a nonvanishing expectation value of the charge fluctuations and circulating loop currents in the cQSL phase[35]. In fact, such features are expected in spin liquid systems[44–46]. The relevant operators for the charge fluctuations and loop currents in the TLHM read[35]

$$\delta\hat{\boldsymbol{\rho}}_{i,jk} = e\frac{8t^3}{U^3}\left(\mathbf{S}_i \cdot \mathbf{S}_j + \mathbf{S}_i \cdot \mathbf{S}_k - 2\mathbf{S}_j \cdot \mathbf{S}_k\right), \quad (9)$$

$$\hat{\mathcal{I}}_{ij,k} = \hat{\mathbf{r}}_{ij}\frac{24e}{\hbar}\frac{t^3}{U^2}\mathbf{S}_k \cdot \left(\mathbf{S}_i \times \mathbf{S}_j\right), \quad (10)$$

where $\langle ijk\rangle$ denotes an elementary triangle in the lattice, e is the electronic charge, $\hat{\mathbf{r}}_{ij}$ is the unit vector along the bond $\langle ij\rangle$. The forms of $\delta\hat{\boldsymbol{\rho}}_{i,jk}$ and $\hat{\mathcal{I}}_{ij,k}$ are uniquely determined by the transformation of these quantities with respect to the following symmetry operations: SU(2) spin rotation, TRS, and inversion operation.

We now compute the expectation values of the above operators in the spinon ground state. In this regard, we construct the real space spinon Hamiltonian on a finite system of linear size $L = 30$ and obtain the eigenvalues of the corresponding eigenfunctions of the $2L^2 \times 2L^2$ Hamiltonian (see the Supplementary Material for more details). At first, we rewrite the above operators in Eqs. (9) and (10) in the spinon degrees of freedom using the same mean-field decomposition as in section "Results." For explicit numerical analysis, we need to fix the mean-field parameters. For subsequent analysis in this section, we work in units of $\tilde{t} = 1$. This leads to a solution of m_0 in terms of $\tilde{J}$, and $\tilde{J}_\chi$ from Eq. (8) as $\frac{3m_0}{4} = -\tilde{J}/\tilde{J}_\chi \pm \sqrt{\tilde{J}^2 + 3\tilde{J}_\chi}/\tilde{J}_\chi$. Next, we rewrite Eqs.

(9) and (10) in mean-field decomposition as

$$\delta\hat{\boldsymbol{\rho}}_{i,jk} = \rho_0\left(e^{i\phi_{ji}}f_i^\dagger f_j + e^{i\phi_{ki}}f_i^\dagger f_k - 2e^{i\phi_{kj}}f_j^\dagger f_k\right) + \text{h.c.},$$

$$\hat{\mathcal{I}}_{ij,k} = \mathcal{I}_0 i e^{i(\phi_{ik} + \phi_{kj})}f_j^\dagger f_i + \text{h.c.} + \text{permute }\{i,j,k\}, \quad (11)$$

where $\rho_0 = e\frac{8m_0 t^3}{U^3}$, and $\mathcal{I}_0 = \hat{\mathbf{r}}_{ij}\frac{e}{\hbar}\frac{9m_0^2 t^3}{U^2}$ are parameters that depend on the amplitude of the mean-field. Note that we added the contributions of the spin degrees of freedom in Eq. (11) (see the Supplementary Material for more details) because of the degenerate spin bands and hence skipped the spin indices.

To obtain the total charge fluctuation and the loop current for a particular site or a bond, we need to add the contributions of all the shared triangles[35,46]. Utilizing the mean-field expressions in Eq. (11) for the relevant operators, we calculate their expectation values in the spinon ground state (see the Supplementary Material for more details) for a finite system, as mentioned earlier. The numerical estimates converge beyond the linear size $L \sim 20$. In the periodic boundary conditions (PBC), each isolated triangle leads to identical estimates for the charge fluctuation and loop current expectation values. Consequently, there are no charge redistributions or circulating loop currents in the cQSL ground state. However, we obtain novel localized charge profiles and loop currents around the system's edges in a finite system i.e. with open boundary conditions (OBC). The corresponding results are shown in Fig. 3a. The arrows around the edge signify the magnitude and direction of the localized currents. All values are in units of $2|\mathcal{I}_0|$. The magnitude of the loop currents is slightly larger (~0.7145) around the corners [C_1 in Fig. 3a] which are formed by either an up or down triangle, whereas they are smaller (~0.6338) around corners which are composed of both an up and a down triangle [C_2 in Fig. 3a]. Note that the loop currents quickly saturate (~0.6764) as we move away from the corners along the edges and are consistent with the inversion and C_6 rotation symmetries.

Similarly, a finite charge fluctuation redistributes localized charges around the system's edges, as shown by blue and red circles. In this case, all numbers are shown in units of $2\rho_0$. Like the loop currents, the charge profile quickly saturates away from the corners. The maximum charge fluctuations (+0.0217/−0.0185) occur around the corner C_1, whereas the minimum fluctuation (+0.0201/−0.0163) occurs around the corners C_2. The key feature is that the smaller the number of shared triangles for a particular site or a bond, the more the corresponding charge fluctuations or localized currents are, respectively. Most interestingly, the charge separation around the edges leads to the formation of a unique dipole moment distribution that can be observed experimentally.

Case of a localized spinon

The cQSL supports spinons as its low-energy excitation. At the sample edge, there exists a gapless chiral spinon edge mode due
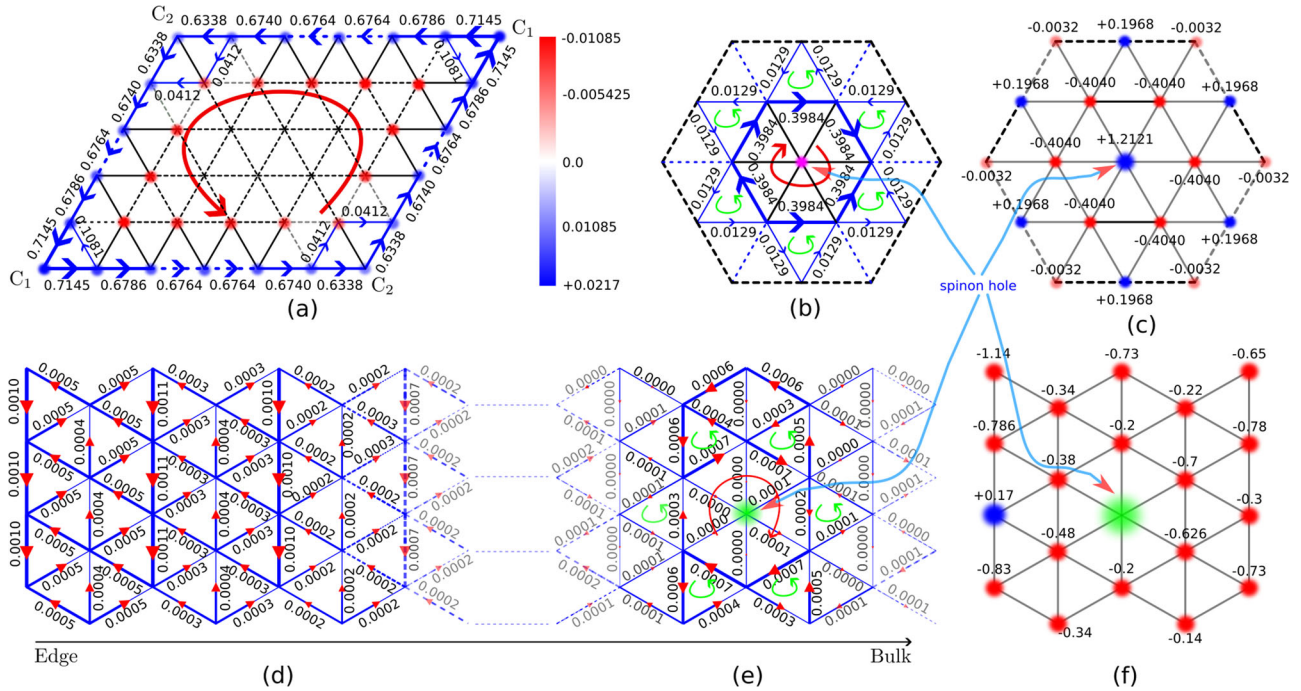
Fig. 3 Localized loop current and charge distributions in the chiral quantum spin liquid. a An illustration of the localized loop current and charge distributions around the edge of a finite system of linear size $L = 30$ (in open boundary condition) within the mean-field spinon description of the spin model in Eq. (3). For illustrative purposes, we do not show the explicit distribution of the loop currents within the bulk. Note that the loop current and charge fluctuation quickly vanish after a few lattice spacings inside the bulk. The loop currents (**b**) and charge distribution (**c**) around the localized spinon hole site were obtained in periodic boundary conditions with the same system size. Red and blue signify opposite signs of charge redistribution. The numbers are presented in units of $2\mathcal{I}_0$ and $2\rho_0$, respectively (see the main text). **d, e** Plots of the local electric currents on the triangular Hubbard model for **d** without and **e** with a spinon hole located at the position labeled by the green color obtained by the DMRG calculations. The loop current emerges around the local magnetic field. The red arrows represent the direction of the loop current. The numbers around the bonds label the absolute value of the current in units of $et/\hbar$. **f** Plot of the charge redistribution around the local spinon hole on a finite-size system (illustrated by the green region) obtained by the DMRG calculations. For clarity, the numbers are in units of $10^{-4}e$. Note that the triangular lattices are rotated by 90° between the top and bottom panels, for *illustrative* purposes only.

to the non-trivial topology of the spinon bands. However, the spinon excitations are gapped inside the bulk. In a clean system with translational invariance in bulk, there are no charge fluctuations or loop currents in bulk [see Fig. 3a]. Here we focus on an isolated/localized spinon excitation in bulk and discuss its associated electromagnetic responses.

In a clean cQSL, the lower spinon bands with spin up and down are fully occupied. To create a spinon hole, we demand that a specific spin in the spin Hamiltonian does not participate in fractionalization into spinons. In the mean-field description, this can be achieved by setting the chemical potential for spinons at the pinning site [see Fig. 3b, c] to be high so that spinons will not occupy the defect site within the low-energy dynamics. This creates a localized spinon hole at the pinning site. Now, we consider a system as before with the defect formed by a large chemical potential at the pinning site, as shown in Fig. 3b, c, and impose periodic boundary conditions (PBC). Performing a similar analysis as in section "Analysis" (See the Supplementary Material for more details), we notice a redistribution of the charge profile around the localized spinon hole and a build-up of localized circulating loop current [see Fig. 3b, c]. As before, all the numbers for charge and current are in units of $2\rho_0$ and $2|\mathcal{I}_0|$, respectively. We notice that the circulating loop current around the spinon hole site has the opposite chirality compared to the loop current flowing along the edge [see Fig. 3a] in the clean system with OBC. On the other hand, dipole moments formed by the charge redistribution are anti-aligned with the edge dipole moments in the clean system. In the latter case, we only focus on the nearest-

neighbor location around the pinning site. Note that the charge profile quickly vanishes away from the pinning center.

DMRG calculations

To validate the above mean-field calculations, we next study the TLHM at an intermediate coupling [Eq. (2)] by using an unbiased DMRG method, and compare the numerical results with our phenomenological model in Eq. (3). Our DMRG calculations are based on the 4-leg cylinder with length $L = 64$. We retain up to bond dimensions $D = 4800$ U(1) states in the DMRG calculations, and we ensure that the main numerical features shown below are robust by tuning the bond dimension from $D = 1200$ to 4800. We summarize our DMRG results in Fig. 3d, e with $U = 10t$, i.e., deep in the cQSL regime. Here, we show the left half of the cylinder for simplicity. We identify that the persistent electric current exists only close to the boundary, manifested by the nontrivial topology and spontaneous TRS breaking of the cQSL phase. The local electrical current quickly reduces from the boundary to the bulk. In the deep bulk, the net current is vanishingly small.

To create a spinon hole, we can add a local magnetic field $H_{loc} = V_i(n_{i\uparrow} - n_{i\downarrow})$ to the Hamiltonian Eq. (2). (In practice, we add two local magnetic fields and ensure that they are separated far away. One pinning point is shown as the green dot in Fig. 3e, and the other is in the other half of the cylinder, which is not shown here.) Note that, introducing local magnetic fields explicitly breaks the translational symmetry along the cylinder circumference direction, so one cannot use the translational symmetry to boost the DMRG calculations. The local magnetic field pins the spin locally and forbids it from fractionalizing into delocalized spinons,

thus creating a spinon hole. Around the spinon hole, nonzero electric currents emerge in bulk. Importantly, around the pinned spinon hole, we identify the formation of a loop current (as indicated by the dashed arrow). It is also clear that the electrical charge distribution deviates from the average filling 1 required for the Mott insulator, as shown in Fig. 3c, e. The general picture of this loop current and charge distribution associated with a spinon hole agrees with the prediction of the mean-field calculations in section "Case of a localized spinon." Due to the finite-size effect in the narrow direction in the DMRG calculations, the current and charge distribution do not respect C_6 rotation symmetry along the spinon.

Numerical estimates. The DMRG results allow us to estimate the magnitude of the mean-field order parameter m_0. First, we provide a rough estimate of $\tilde{J}, \tilde{J}_\chi$ in Eq. (3) based on ref. [17] and Supplementary Material. Inserting characteristic values (also used in our DMRG calculations) such as $t = 1$ eV, $U = 10$ eV, and $\chi \sim -0.35$ [17], we obtain $\tilde{J} \sim 0.37$ eV and $\tilde{J}_\chi \sim 0.15$ eV. Note that the absolute value of χ is larger than its classical upper limit, i.e. $\frac{1}{8}$. However, the estimate obtained from our DMRG and also supported by ref. [17] provides $|\chi| \sim 0.35$. We anticipate that such a large departure of the absolute value of χ from its classical limit is a consequence of large quantum fluctuations which are unavoidably present away from the antiferromagnetic phase transition. Here, χ is the nonzero chiral order parameter as defined in Fig. 1. Since the eigenfunctions of the Hamiltonian in Eq. (5) do not depend on the magnitude of $\tilde{t}$, we can compare the loop current magnitudes around the edge of the system obtained by DMRG with our mean-field analysis. Our estimates provide a mean-field amplitude $m_0 \sim 0.1$. Using this in Eq. (8), we obtain an order of magnitude for our phenomenological hopping parameter $\tilde{t} \sim 0.02$ eV. Plugging in the magnitude (obtained by DMRG) of the enclosed loop current around our localized spinons, we estimate an emergent orbital magnetization $\sim 0.01 \, \mu_B$, where μ_B is the Bohr magneton.

Quantum field theory description
The orbital electrical current associated with a spinon can also be understood from the quantum field theory perspective, which sheds further light on the origin of the orbital electrical current. One hallmark of the QSL is the fractionalization of spins and the appearance of an emergent gauge field. Understanding the coupling between the emergent gauge field and the physical electromagnetic fields is crucial for the electromagnetic detection of the QSL. In terms of the parton description, the electron operator can be written as $c_\sigma = b f_\sigma$, where b is a boson operator that carries the electron charge e, and f_σ is a fermionic spinon operator that carries the spin-$\frac{1}{2}$. In cQSL, f_σ fermions form Chern bands as was shown in section "Results." The fractionalization dictates that the charged boson is coupled to both the physical gauge field $\mathbf{A}$ and an emergent gauge field $\mathbf{a}$ as $b \to b \exp[i(A - a)]$, while the spinon is coupled only to the emergent gauge field as, $f_\sigma \to f_\sigma \exp(ia)$. The effective low-energy Lagrangian for the b boson has the standard Ginzburg–Landau form (we use the unit $\hbar = e = c = 1$) [46–48]

$$\mathcal{L}_b = \sum_{\mu=x,y} |(i\partial_\mu + a_\mu - A_\mu)b|^2 - g|b|^2 - \frac{u}{2}|b|^4 + \cdots. \quad (12)$$

b boson is gapped with $g > 0$ in the cQSL which is a Mott insulator. However, there is still a diamagnetic response in $\mathbf{A} - \mathbf{a}$ due to the local current loop in the presence of a magnetic field, similar to Landau diamagnetism in metal, although the current loops are strongly localized. Since the b boson is gapped, we can integrate it out to obtain an effective Lagrangian as

$$\mathcal{L} = \frac{2C}{4\pi}\epsilon^{\mu\nu\rho}a_\mu\partial_\nu a_\rho - \frac{\chi_b}{2}[\nabla\times(\mathbf{a}-\mathbf{A})]^2 - \frac{\chi_B}{2}(\nabla\times\mathbf{A})^2, \quad (13)$$

where the first term on the right-hand side is the Chern-Simon term obtained by integrating out f_σ that fills topological Chern bands with a Chern number C ($C = 1$ in our model). Here, χ_b accounts for the diamagnetic susceptibility due to the gapped boson b, χ_B is the susceptibility of the background [49]. It is clear from the Chern-Simon term that a spinon carries π/C flux of $\mathbf{a}$ [50]. The physical magnetic field associated with the emergent magnetic field, which can be seen in Eq. (13) by minimizing $\mathcal{L}$ with respect to $\mathbf{B} \equiv \nabla \times \mathbf{A}$, is: $\mathbf{B} = \chi_b/(\chi_b + \chi_B) \nabla \times \mathbf{a}$. Hence, a spinon excitation induces an orbital electrical current with a total flux of $\mathbf{B}$ equal to $\chi_b\pi/(\chi_b + \chi_B)C$.

Dynamic spin-structure factor
In the previous sections, we established that spinon excitations in the cQSL phase carry orbital electrical loop currents and charges. Now, we proceed to investigate the electromagnetic response of a cQSL in terms of optical conductivity and Faraday rotation. Before considering the optical conductivity, which involves higher-order spinon correlation functions, we consider the standard dynamic spin-structure factor (DSSF) in the framework of spinon description. DSSF is an essential physical quantity that is routinely used as an experimental tool to probe the nature of the magnetic ground state and is defined as

$$S(\mathbf{q}, \omega) = \sum_{i,j} \frac{e^{i\mathbf{q}\cdot(\mathbf{r}_i - \mathbf{r}_j)}}{N_s} \int_{-\infty}^{\infty} dt e^{i\omega t} \langle \mathbf{S}_i(t) \cdot \mathbf{S}_j(0)\rangle, \quad (14)$$

where N_s denotes the number of sites, and $\mathbf{q}, \omega$ denotes the probe momentum and frequency, respectively. With the two-sublattice structure as illustrated in Fig. 2a, we first rewrite Eq. (14) in terms of spinon operators. The above expression simplifies upon utilizing the spectral representation with the weighted summation over the sub-lattice resolved spin-structure factors. The latter is written as (see the Supplementary Material for more details)

$$S^{\eta\zeta}(\mathbf{q}, \omega) = \frac{3}{2} \sum_{n,\mathbf{k}} \left\langle 0|f_{\eta,\mathbf{k}}^\dagger f_{\eta,\mathbf{k}+\mathbf{q}}|n\right\rangle \left\langle n|f_{\zeta,\mathbf{k}+\mathbf{q}}^\dagger f_{\zeta,\mathbf{k}}|0\right\rangle \delta(\omega - E_n + E_0),$$
$$\{\eta, \zeta\} \in \text{A}, \text{B}$$
$$(15)$$

where {A, B} denotes the two sublattice degrees of freedom, and E_n denotes the eigen energy of the n-th excited state. Note that we added the contributions from the degenerate spin up and down bands, and consequently skipped the indices as before. Rewriting in the diagonal basis and summing the sublattice degrees of freedom, we obtain the DSSF in our phenomenological cQSL. In Fig. 4b, we show the DSSF profile. Note that we have adopted a normalization where the absolute maximum is set to unity for convenience. The excited state $|n\rangle$ contains one pair of spinon hole and spinon excitation, or spinon exciton, as evident from Eq. (15).

We notice that apart from a relatively strong peak centered in a narrow region around the edge of the BZ at the K point, there are almost no sharp features within the BZ. The broad continuum in the BZ reflects the absence of any long-range magnetic order, i.e., there are no well-defined magnon excitations at a given momentum $\mathbf{q}$ with energy ω. The relatively broad/diffused bands (illustrated by the white halos) correspond to a two-spinon continuum. At $\mathbf{q} = 0$, the DSSF corresponds to the vertical spinon exciton, as is evident from Eq. (15). In this case, the wave function overlap between the wave function of the spinon hole in the occupied band and the spinon in the unoccupied band is zero at the same momentum and subsequently leads to a vanishing weight distribution around the Γ point, as seen in Fig. 4b. To illustrate this, we also plot the scattering density of states $g(\omega, \mathbf{q}) = \sum_\mathbf{k}\delta(\omega - \varepsilon_{\mathbf{k}+\mathbf{q}} - \mathbf{q})$ in Fig. 4a, where there is a finite spectral weight around the Γ point. The absence of spectral weight around the Γ point is common to the cQSL phase in other lattices,
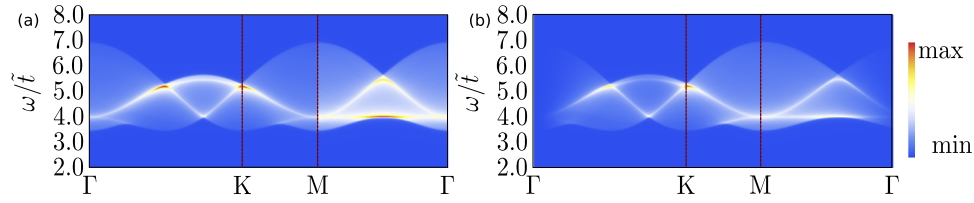
Fig. 4 Normalized scattering density of states and the dynamic spin structure factor in the chiral quantum spin liquid. The normalized scattering density of states $g(\mathbf{q}, \omega)$ (**a**) (see definition in the main text) and the dynamic spin structure factor $S(\mathbf{q}, \omega)$ (**b**) along the high symmetry points of the triangular lattice Brillouin zone (BZ). The analysis is performed neglecting any spinon interactions which are present when the dynamics of the emergent gauge field are considered explicitly.
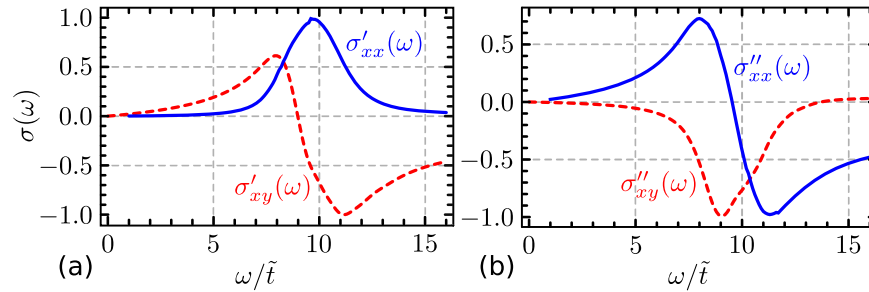
Fig. 5 Calculated optical conductivity in the chiral quantum spin liquid. The real (**a**) and the imaginary (**b**) part of the normalized transverse (*dashed line*) and longitudinal (*solid line*) optical conductivity as a function of the frequency of the incident light.

viz. kagome[51,52]. In reality, the fluctuations of the emergent gauge field around the mean-field saddle point mediate the attraction between the spinon hole and the spinon, which has been neglected in the present discussion. However, even in that case, the spectral weight around the Γ point will vanish due to the zero overlap of the eigenfunctions[51].

Optical conductivity and Faraday rotation

Finally, we focus on the main result of our work by showing that optical responses below the Mott gap can be used to probe the emergent cQSL state in the TLHM[44,53,54]. The longitudinal and transverse optical conductivity in this regime become nonvanishing because of the finite electronic polarization. Following the work by Bulaevskii et al.[35], we obtain the corresponding expression for a three-site problem as

$$P_x = 4\sqrt{3}ea\frac{t^3}{U^3}\left(\mathbf{S}_i \cdot \mathbf{S}_j + \mathbf{S}_i \cdot \mathbf{S}_k - 2\mathbf{S}_j \cdot \mathbf{S}_k\right), \quad (16)$$

$$P_y = 12ea\frac{t^3}{U^3}\left(\mathbf{S}_i \cdot \mathbf{S}_j - \mathbf{S}_i \cdot \mathbf{S}_k\right), \quad (17)$$

where a is the lattice constant, and t, U are the parameters defined as before in Eq. (2). The above two expressions are particularly relevant as we deal with a triangle lattice. However, note that within a lattice framework we need to add the contributions of all the triangles surrounding a particular site i to obtain the total polarization $\mathbf{P}$. The latter naturally couples to an external electric field as $-\mathbf{P} \cdot \mathbf{E}(t)$. Consequently, the associated optical conductivity within the linear response theory reads[54–56]

$$\sigma_{ab}(\omega) = \frac{i\omega}{V\hbar}\sum_{n\neq 0}\frac{\langle\psi_0|P_a|\psi_n\rangle\langle\psi_n|P_b|\psi_0\rangle}{\omega - \omega_n + i\epsilon} + \frac{a \leftrightarrow b}{\omega_n \to -\omega_n}, \quad (18)$$

where $|\psi_0\rangle$, and $|\psi_n\rangle$ are the ground and excited states, respectively, $\mathcal{H}|\psi_n\rangle = E_n|\psi_n\rangle \forall n \in \{0, 1, 2, \dots\}$, V is the volume, and $\omega_n = E_n - E_0$, where E_0 is the energy of the ground state. Note that the above expression is valid in the frequency regime much less than the energy scale (U) associated with the charge gap in the Hubbard model, i.e. $\hbar\omega \ll U$. Additionally, broken TRS in the chiral phase immediately implies non-vanishing off-diagonal components ($a \neq b$). This leads to a finite MOFE signal proportional

to the real part of the transverse optical conductivity defined in Eq. (1).

We proceed as before in section "Dynamic spin-structure factor" by rewriting the polarization operator in terms of spinon degrees of freedom. Readers are referred to Supplementary Materials for the details of the calculations. However, in stark contrast to the DSSF analysis, here we need to consider the correlation functions involving eight spinon operators, as is evident from Eq. (18) (see the Supplementary Material for more details). We perform numerical integration in Mathematica with a quasi-Monte Carlo routine and obtain the transverse and longitudinal optical conductivity as a function of the frequency as shown in Fig. 5. Both the real (σ') and imaginary (σ'') parts of the quantities are shown in panel (a) and panel (b), respectively. Similar to section "Dynamic spin-structure factor," we adopted a normalization in which the absolute maximum of the quantities is set to unity.

We notice that $\sigma'_{xy}(\omega)$ changes sign at a frequency $\omega_0 \sim 9\tilde{t}$ that is almost twice the spinon gap around the BZ edge at the M point. Around the same frequency $|\sigma''_{xy}(\omega)|$ attains its largest magnitude. $\sigma'_{xx}(\omega)$, and $\sigma''_{xx}(\omega)$ also show similar characteristics at frequencies close to twice the spinon gap at the M point. Plugging in characteristic numbers [aimed towards κ-(BEDT)Cu$_2$(CN)$_3$] as $t = -0.05$ eV, $U = 10$ eV, $m_0 \sim 0.1$, $a \sim 10$ Å, and $\tilde{t} \sim 0.02$ eV, we obtain $\sigma'_{xy} \sim \times 10^{-10}\frac{e^2}{\hbar}$ for $\omega \sim 20$ THz. This leads to an estimated Faraday rotation angle of around 20 nRad/μm per thickness of the sample. The magnitude is probably slightly beyond the allowed resolution of current experiments[57]. Our results suggest that Mott insulators with a larger t are beneficial for a stronger MOFE signal.

DISCUSSION

This paper provides extensive mean-field analysis for the electromagnetic response of a cQSL phase. We started from a phenomenological cQSL Hamiltonian as in Eq. (3) and analyzed the spectrum of fractionalized excitations in terms of spinon mead field theory. Despite being deep inside the Mott insulator regime, where the charge degrees of freedom are gapped, we obtain a nonvanishing electrical loop current distribution and charge fluctuations associated with a localized spinon excitation. Additionally, we performed unbiased DMRG calculations in the triangular lattice Hubbard model at the intermediate coupling

regime, where the cQSL is stabilized. The DMRG results confirm the physical picture of the parton mean-field results, where both approaches provide similar structures of the loop currents and charge redistributions in the cQSL phase, as illustrated in Fig. 3. The DMRG calculations further allow us to estimate the magnitude of the electrical charge and orbital current associated with a spinon excitation. Assuming a typical value of $t = 1$ eV and $U = 10$ eV, we estimate the electrical current and charge around the localized spinons to be around 17 μA, and $\pm 0.1\%$ of e, respectively. In addition, we performed quantum field theory analysis to unravel the connection between the spinon excitation and emergent and physical gauge fields, which clearly shows that a flux of the physical magnetic field dresses a localized spinon.

The electromagnetic characteristics of spinon excitations immediately imply a nonvanishing optical response in the cQSL. We compute the optical response functions by focusing on the optical conductivity. The nonvanishing transverse optical conductivity $\sigma'_{xy}(\omega)$ below the Mott gap can be considered a smoking gun signature of the underlying chiral nature of the QSL. Note that the finite transverse optical conductivity along with the absence of any long-range magnetic order as illustrated by the structure factor [no sharp features] is considered as a clear evidence for the cQSL in the TLHM. Since a finite $\sigma'_{xy}(\omega)$ signifies a non-zero Faraday rotation angle Θ_F, our predictions can be directly tested by suitable optical techniques such as MOFE or Kerr effect. Since $\sigma'_{xy}(\omega)$ changes sign as the frequency increases, an experimental signature of cQSL would be to see if, as a function of incoming photon frequency, the Faraday rotation angle changes sign or not. For completeness and as an intermediate step, we also analyze the dynamic spin-structure factor of the cQSL as illustrated in Fig. 4b. The absence of sharp features signifies no well-defined magnon excitations in the QSL. Of course, an external magnetic will be break the TRS and may lead to a finite transverse optical conductivity. However, the key message of our proposal is that the TLHM in the intermediate coupling supports finite transverse optical conductivity even in the absence of any external TRS-breaking fields due to the emergence of cQSL.

In cQSL, each unit triangle carries an orbital current. However, this orbital current cancels in the bond shared by two neighboring triangles for a translationally invariant system. This cancelation is not perfect in the presence of impurities or near edges, leaving finite orbital magnetization localized around impurities. Therefore, the orbital magnetization localized around impurities already serves as a signature of time-reversal symmetry breaking in QSL. This defect-induced orbital magnetization can be distinguished from spinons, which are dynamical excitations (despite being gapped) of cQSL. Depending on the protocol to tune the system into the cQSL, spinons can be created at different system locations, and the protocol can control their density. On the contrary, the orbital magnetization localized around impurities does not depend on the protocol.

Compared to our previous theoretical work on Kitaev materials[46], here, TRS is spontaneously broken due to considerable charge fluctuations in a Hubbard model at intermediate coupling strength. As noted in our quantitative estimates for the loop current or associated charge polarization, the latter translates into a larger electromagnetic response. Note that the associated gauge structure for the cQSL in the TLHM is U(1), whereas the Kitaev spin liquid has a Z_2 gauge structure. Recently, a few theoretical works have proposed experimental probes of the Kitaev spin liquid via NV center magnetometry[58] or spin-polarized STM[59]. Meanwhile, spinon Fermi surface induced transverse conductivity has been proposed to be hallmark signatures for U(1) QSLs[60,61]. Our proposal to detect the cQSL phase based on the electromagnetic signatures closely complements them.

In summary, we show that spinon excitations in cQSL carry an electrical charge and orbital current, despite the system being a Mott insulator. Such an electromagnetic response can be detected experimentally using the MOFE or Kerr effect. Therefore, our work provides a clear electromagnetic signature of the cQSL, which helps determine the nature of non-magnetic states observed in certain materials realizing the triangular lattice Mott insulator.

DATA AVAILABILITY

The data that support the findings of this study are available from the corresponding authors on reasonable request. The DMRG code developed by the authors is distributed upon proper request.

REFERENCES

1. Anderson, P. W. Resonating valence bonds: a new kind of insulator? *Mater. Res. Bull.* **8**, 153–160 (1973).
2. Broholm, C. et al. Quantum spin liquids. *Science* **367**, 263–272 (2020).
3. Zhou, Y., Kanoda, K. & Ng, T.-K. Quantum spin liquid states. *Rev. Mod. Phys.* **89**, 025003 (2017).
4. Kitaev, A. Anyons in an exactly solved model and beyond. *Ann. Phys.* **321**, 2–111 (2006).
5. Savary, L. & Balents, L. Quantum spin liquids: a review. *Rep. Prog. Phys.* **80**, 016502 (2016).
6. Nica, E. M., Akram, M., Vijayvargia, A., Moessner, R. & Erten, O. Kitaev spin-orbital bilayers and their moiré superlattices. *npj Quantum Mater.* **8**, 9 (2023).
7. Kumar, U., Banerjee, S. & Lin, S.-Z. Floquet engineering of Kitaev quantum magnets. *Commun. Phys.* **5**, 157 (2022).
8. Banerjee, S., Kumar, U. & Lin, S.-Z. Inverse Faraday effect in Mott insulators. *Phys. Rev. B* **105**, L180414 (2022).
9. Semeghini, G. et al. Probing topological spin liquids on a programmable quantum simulator. *Science* **374**, 1242–1247 (2021).
10. Satzinger, K. J. et al. Realizing topologically ordered states on a quantum processor. *Science* **374**, 1237–1241 (2021).
11. Miyashita, S. A variational study of the ground state of frustrated quantum spin models. *J. Phys. Soc. Jpn.* **53**, 44–47 (1984).
12. Huse, D. A. & Elser, V. Simple variational wave functions for two-dimensional Heisenberg spin-$\frac{1}{2}$ antiferromagnets. *Phys. Rev. Lett.* **60**, 2531–2534 (1988).
13. Bernu, B., Lhuillier, C. & Pierre, L. Signature of Néel order in exact spectra of quantum antiferromagnets on finite lattices. *Phys. Rev. Lett.* **69**, 2590–2593 (1992).
14. Capriotti, L., Trumper, A. E. & Sorella, S. Long-range Néel order in the triangular Heisenberg model. *Phys. Rev. Lett.* **82**, 3899–3902 (1999).
15. Hu, W.-J., Gong, S.-S., Zhu, W. & Sheng, D. N. Competing spin-liquid states in the spin-$\frac{1}{2}$ Heisenberg model on the triangular lattice. *Phys. Rev.* **92**, 140403 (2015).
16. Sorella, S., Otsuka, Y. & Yunoki, S. Absence of a spin liquid phase in the Hubbard model on the honeycomb lattice. *Sci. Rep.* **2**, 992 (2012).
17. Szasz, A., Motruk, J., Zaletel, M. P. & Moore, J. E. Chiral spin liquid phase of the triangular lattice Hubbard model: a density matrix renormalization group study. *Phys. Rev. X* **10**, 021042 (2020).
18. Cookmeyer, T., Motruk, J. & Moore, J. E. Four-spin terms and the origin of the chiral spin liquid in Mott insulators on the triangular lattice. *Phys. Rev. Lett.* **127**, 087201 (2021).
19. Zhu, Z., Sheng, D. N. & Vishwanath, A. Doped Mott insulators in the triangular-lattice Hubbard model. *Phys. Rev. B* **105**, 205110 (2022).
20. Chen, B.-B. et al. Quantum spin liquid with emergent chiral order in the triangular-lattice Hubbard model. *Phys. Rev. B* **106**, 094420 (2022).
21. Kadow, W., Vanderstraeten, L. & Knap, M. Hole spectral function of a chiral spin liquid in the triangular lattice Hubbard model. *Phys. Rev. B* **106**, 094417 (2022).
22. Kalmeyer, V. & Laughlin, R. B. Equivalence of the resonating-valence-bond and fractional quantum Hall states. *Phys. Rev. Lett.* **59**, 2095–2098 (1987).
23. Nikolaev, S. A., Solovyev, I. V. & Streltsov, S. V. Quantum spin liquid and cluster Mott insulator phases in the Mo_3O_8 magnets. *npj Quantum Mater.* **6**, 25 (2021).
24. Shimizu, Y., Miyagawa, K., Kanoda, K., Maesato, M. & Saito, G. Spin liquid state in an organic Mott insulator with a triangular lattice. *Phys. Rev. Lett.* **91**, 107001 (2003).
25. Itou, T., Oyamada, A., Maegawa, S., Tamura, M. & Kato, R. Quantum spin liquid in the spin-$\frac{1}{2}$ triangular antiferromagnet $\frac{1}{2}$. *Phys. Rev. B* **77**, 104413 (2018).
26. Miksch, B. et al. Gapped magnetic ground state in quantum spin liquid candidate $\kappa - (BEDT - TTF)_2 - Cu_2(CN)_3$. *Science* **372**, 276–279 (2021).
27. Pustogow, A. Thirty-year anniversary of $\kappa - (BEDT - TTF)_2 - Cu_2(CN)_3$: reconciling the spin gap in a spin-liquid candidate. *Solids* **3**, 93–110 (2022).
28. Li, Y. et al. Gapless quantum spin liquid ground state in the two-dimensional spin-1/2 triangular antiferromagnet $YbMgGaO_4$. *Sci. Rep.* **5**, 16419 (2015).
29. Ding, L. et al. Gapless spin-liquid state in the structurally disorder-free triangular antiferromagnet $NaYbO_2$. *Phys. Rev. B* **100**, 144432 (2019).

30. Bordelon, M. M. et al. Field-tunable quantum disordered ground state in the triangular-lattice antiferromagnet NaYbO$_2$. *Nat. Phys.* **15**, 1058–1064 (2019).

31. Zeng, K. Y. et al. NMR study of the spin excitations in the frustrated antiferromagnet Yb(BaBO$_3$)$_3$ with a triangular lattice. *Phys. Rev. B* **102**, 045149 (2020).

32. Sarkar, R. et al. Quantum spin liquid ground state in the disorder free triangular lattice NaYbS$_2$. *Phys. Rev. B* **100**, 241116 (2019).

33. Shen, Y. et al. Evidence for a spinon Fermi surface in a triangular-lattice quantum-spin-liquid candidate. *Nature* **540**, 559–562 (2016).

34. Motrunich, O. I. Orbital magnetic field effects in spin liquid with spinon Fermi sea: possible application to κ-(ET)$_2$Cu$_2$(CN)$_3$. *Phys. Rev. B* **73**, 155115 (2006).

35. Bulaevskii, L. N., Batista, C. D., Mostovoy, M. V. & Khomskii, D. I. Electronic orbital currents and polarization in Mott insulators. *Phys. Rev. B* **78**, 024402 (2008).

36. Delannoy, J.-Y. P., Gingras, M. J. P., Holdsworth, P. C. W. & Tremblay, A.-M. S. Néel order, ring exchange, and charge fluctuations in the half-filled Hubbard model. *Phys. Rev. B* **72**, 115114 (2005).

37. Yoshioka, T., Koga, A. & Kawakami, N. Quantum phase transitions in the Hubbard model on a triangular lattice. *Phys. Rev. Lett.* **103**, 036401 (2009).

38. Sahebsara, P. & Sénéchal, D. Hubbard model on the triangular lattice: spiral order and spin liquid. *Phys. Rev. Lett.* **100**, 136402 (2008).

39. Yang, H.-Y., Läuchli, A. M., Mila, F. & Schmidt, K. P. Effective spin model for the spin-liquid phase of the Hubbard model on the triangular lattice. *Phys. Rev. Lett.* **105**, 267204 (2010).

40. Mezio, A., Sposetti, C. N., Manuel, L. O. & Trumper, A. E. A test of the bosonic spinon theory for the triangular antiferromagnet spectrum. *EPL* **94**, 47001 (2011).

41. Flint, R. & Coleman, P. Symplectic *N* and time reversal in frustrated magnetism. *Phys. Rev. B* **79**, 014424 (2009).

42. Fukui, T., Hatsugai, Y. & Suzuki, H. Chern numbers in discretized Brillouin zone: efficient method of computing (spin) Hall conductances. *J. Phys. Soc. Jpn.* **74**, 1674–1677 (2005).

43. Nakai, R., Ryu, S. & Nomura, K. Finite-temperature effective boundary theory of the quantized thermal Hall effect. *New J. Phys.* **18**, 023038 (2016).

44. Potter, A. C., Senthil, T. & Lee, P. A. Mechanisms for sub-gap optical conductivity in herbertsmithite. *Phys. Rev. B* **87**, 245106 (2013).

45. Pereira, R. G. & Egger, R. Electrical access to Ising anyons in Kitaev spin liquids. *Phys. Rev. Lett.* **125**, 227202 (2020).

46. Banerjee, S. & Lin, S.-Z. Emergent orbital magnetization in Kitaev quantum magnets. *SciPost Phys.* **14**, 127 (2023).

47. Chowdhury, D., Sodemann, I. & Senthil, T. Mixed-valence insulators with neutral Fermi surfaces. *Nat. Commun.* **9**, 1766 (2018).

48. Lee, S.-S. & Lee, P. A. U(1) gauge theory of the Hubbard model: spin liquid states and possible application to (BEDT-TTF)$_2$Cu$_2$(CN$_3$). *Phys. Rev. Lett.* **95**, 036403 (2005).

49. Sodemann, I., Chowdhury, D. & Senthil, T. Quantum oscillations in insulators with neutral Fermi surfaces. *Phys. Rev. B* **97**, 045152 (2018).

50. Lin, S.-Z. Kondo enabled transmutation between spinons and superconducting vortices: origin of magnetic memory in 4Hb-TaS$_2$. Preprint at https://arxiv.org/abs/2210.06550 (2022).

51. Punk, M., Chowdhury, D. & Sachdev, S. Topological excitations and the dynamic structure factor of spin liquids on the kagome lattice. *Nat. Phys.* **10**, 289–293 (2014).

52. Halimeh, J. C. & Punk, M. Spin structure factors of chiral quantum spin liquids on the kagome lattice. *Phys. Rev. B* **94**, 104413 (2016).

53. Colbert, J. R., Drew, H. D. & Lee, P. A. Magneto-optical Faraday effect in spin-liquid candidates. *Phys. Rev. B* **90**, 121105 (2014).

54. Hwang, K., Bhattacharjee, S. & Kim, Y. B. Signatures of spin-triplet excitations in optical conductivity of valence bond solids. *New J. Phys.* **16**, 123009 (2014).

55. Mahan, G. D. *Condensed Matter in a Nutshell* (Princeton University Press, 2011).

56. Marder, M. P. *Condensed Matter Physics* (Wiley, 2010).

57. Jenkins, G. S. et al. Giant plateau in the terahertz Faraday angle in gated Bi$_2$Se$_3$. *Phys. Rev. B* **86**, 235133 (2012).

58. Chatterjee, S., Rodriguez-Nieva, J. F. & Demler, E. Diagnosing phases of magnetic insulators via noise magnetometry with spin qubits. *Phys. Rev. B* **99**, 104425 (2019).

59. He, W.-Y. & Lee, P. A. Electronic density of states of a *U*(1) quantum spin liquid with spinon Fermi surface. II. Zeeman magnetic field effects. *Phys. Rev. B* **107**, 195156 (2023).

60. Khoo, J. Y., Pientka, F., Lee, P. A. & Villadiego, I. S. Probing the quantum noise of the spinon Fermi surface with NV centers. *Phys. Rev. B* **106**, 115108 (2022).

61. Khoo, J. Y., Pientka, F. & Villadiego, I. S. Corrigendum: The universal shear conductivity of Fermi liquids and spinon Fermi surface states and its detection via spin qubit noise magnetometry (2021 New J. Phys. **23** 113009). *New J. Phys.* **24**, 129501 (2022).

ACKNOWLEDGEMENTS

AUTHOR CONTRIBUTIONS

S.B. and S.-Z.L. planned the project. S.B. carried out all the analytical calculations. W.Z. performed the DMRG analysis, and S.-Z.L carried out the field theory analysis. All the authors contributed equally to writing the manuscript.

COMPETING INTERESTS

The authors declare no competing interests.

ADDITIONAL INFORMATION

Supplementary information The online version contains supplementary material available at https://doi.org/10.1038/s41535-023-00595-2.

Correspondence and requests for materials should be addressed to Shi-Zeng Lin.

Reprints and permission information is available at http://www.nature.com/reprints

Publisher's note Springer Nature remains neutral with regard to jurisdictional claims in published maps and institutional affiliations.